

AIAA Atmospheric Flight Mechanics Conference and Exhibit
2-5 August 2010, Toronto, Canada

Flight dynamics properties of 155 mm spin-stabilized projectiles analyzed in different body frames

Dr. Philippe Wernert¹, Dr. Spilios Theodoulis², Dr. Yannick Morel³
French-German Research Institute of Saint-Louis (ISL), 68300 Saint-Louis, France

Flight dynamics properties of 155 mm spin-stabilized projectiles are highlighted in this paper. The 6 Degrees of Freedom (DoF) simulations are performed in rolling and non-rolling body frames by using standard flight mechanics equations. Kinematic features (incidence angles, linear and rotational velocities, ...) as well as histories of forces and moments are illustrated. Special attention is devoted to the calculation and explanation of the aeroballistics incidence polar diagram.

Nomenclature

$[I]$	inertia matrix
(p, q, r)	projectile angular velocity vector components
(u, v, w)	projectile linear velocity vector components
(x, y, z)	projectile location vector components
(α, β)	projectile incidence and sideslip angles
(ψ, θ, ϕ)	projectile Euler angles
DoF	Degree of Freedom
GNC	Guidance, Navigation, Control

Subscripts

b	Ballistics (refers to aeroballistics models)
BR (or B)	Body Rolling (Frame)
BFP	Body Fixed Plane (Frame)
BNS	Body Non Spinning (Frame)
E	Earth (Frame)
F	Frame

I. Introduction

The field of guided ammunitions has received considerable attention in the last years due to increased demands in target hit accuracy and costs reductions. At the French-German Research Institute of Saint-Louis (ISL), several studies related to the topic are under way^{1,2,3,4,5}. In order to be able to derive adequate GNC algorithms, a thorough comprehension of the flight properties of these projectiles is required. In this paper, the flight properties of a 155 mm spin-stabilized projectile launched with a high initial elevation angle are considered and analyzed by means of 6DoF simulations performed in rotating and non-rotating body frames.

¹ Head - GNC Department (Guidance, Navigation, Control), 5, rue du général Cassagnou, philippe.wernert@isl.eu

² GNC Department, 5, rue du général Cassagnou, spilios.theodoulis@isl.eu

³ GNC Department, 5, rue du général Cassagnou, yannick.morel@isl.eu

II. Flight dynamics modeling and body frames

Several frames are needed in order to simulate properly the flight of any flying vehicle:

- A reference frame related to the Earth,
- A frame related to the vehicle velocity,
- A frame related to the vehicle body.

Two kinds of relevant body frames can be defined:

- A body frame rigidly bounded on the projectile. This frame will experience all rotational motions and so, it will be rolling with the projectile.
- A body frame which is not rigidly bounded on the projectile. A very convenient frame is one which experiences the pitching and yawing rotational motions, but not the rolling motion.

In the following, the 6DoF equations of motions in these different body frames will be outlined.

A. Flight mechanics 6 DoF model in the rolling body frame BR

The standard 6DoF translational and rotational equations of motion are written, in the rolling body frame BR, as^{6,7}:

$$\begin{bmatrix} \dot{p} \\ \dot{q} \\ \dot{r} \end{bmatrix} = [I]^{-1} \left(\begin{bmatrix} L \\ M \\ N \end{bmatrix} - \begin{bmatrix} 0 & -r & q \\ r & 0 & -p \\ -q & p & 0 \end{bmatrix} [I] \begin{bmatrix} p \\ q \\ r \end{bmatrix} \right) \quad (1)$$

$$\begin{bmatrix} \dot{\phi} \\ \dot{\theta} \\ \dot{\psi} \end{bmatrix} = \begin{bmatrix} 1 & \sin \phi \tan \theta & \cos \phi \tan \theta \\ 0 & \cos \phi & -\sin \phi \\ 0 & \frac{\sin \phi}{\cos \theta} & \frac{\cos \phi}{\cos \theta} \end{bmatrix} \begin{bmatrix} p \\ q \\ r \end{bmatrix} \quad (2)$$

$$\begin{bmatrix} \dot{u} \\ \dot{v} \\ \dot{w} \end{bmatrix} = \begin{bmatrix} X/m \\ Y/m \\ Z/m \end{bmatrix} + g \begin{bmatrix} -\sin \theta \\ \cos \theta \sin \phi \\ \cos \theta \cos \phi \end{bmatrix} - \begin{bmatrix} 0 & -r & q \\ r & 0 & -p \\ -q & p & 0 \end{bmatrix} \begin{bmatrix} u \\ v \\ w \end{bmatrix} \quad (3)$$

$$\begin{bmatrix} \dot{x}_E \\ \dot{y}_E \\ \dot{z}_E \end{bmatrix} = \begin{bmatrix} \cos \theta \cos \psi & \sin \phi \sin \theta \cos \psi - \cos \phi \sin \psi & \cos \phi \sin \theta \cos \psi + \sin \phi \sin \psi \\ \cos \theta \sin \psi & \sin \phi \sin \theta \sin \psi + \cos \phi \cos \psi & \cos \phi \sin \theta \sin \psi - \sin \phi \cos \psi \\ -\sin \theta & \sin \phi \cos \theta & \cos \phi \cos \theta \end{bmatrix} \begin{bmatrix} u \\ v \\ w \end{bmatrix} \quad (4)$$

The gravity force is written as:

$$\text{Gravity force} \quad \vec{G} = mg \begin{bmatrix} -\sin \theta \\ \cos \theta \sin \phi \\ \cos \theta \cos \phi \end{bmatrix} \quad (5)$$

The components of the aerodynamic forces (X, Y, Z) and moments (L, M, N) acting on the projectile are obtained by means of the following set of relations:

$$\text{Lift force} \quad \vec{L} = \frac{1}{2} \rho S V^2 C_{L\alpha} \begin{bmatrix} \sin^2 \beta + \cos^2 \beta \sin^2 \alpha \\ -\sin \beta \cos \alpha \cos \beta \\ -\cos^2 \beta \sin \alpha \cos \alpha \end{bmatrix} \quad (6)$$

$$\text{Drag force} \quad \vec{D} = -\frac{1}{2} \rho S V^2 C_D \begin{bmatrix} \cos \alpha \cos \beta \\ \sin \beta \\ \sin \alpha \cos \beta \end{bmatrix} \quad (7)$$

$$\text{Magnus force} \quad \vec{K} = \frac{1}{2} \rho S V^2 C_{yp\alpha} \left(\frac{pd}{V} \right) \begin{bmatrix} 0 \\ -\sin \alpha \cos \beta \\ \sin \beta \end{bmatrix} \quad (8)$$

Pitching/yawing moment :

$$\vec{M}_{py} = \frac{1}{2} \rho S d V^2 C_{m\alpha} \begin{bmatrix} 0 \\ \sin \alpha \cos \beta \\ -\sin \beta \end{bmatrix} \quad (9)$$

Magnus moment :

$$\vec{M}_m = \frac{1}{2} \rho S d V^2 (-C_{np\alpha}) \left(\frac{pd}{V} \right) \begin{bmatrix} 0 \\ -\sin \beta \\ -\sin \alpha \cos \beta \end{bmatrix} \quad (10)$$

Pitch/yaw damping moment:

$$\vec{M}_{pyd} = \frac{1}{2} \rho S d V^2 C_{mq} \left(\frac{d}{V} \right) \begin{bmatrix} 0 \\ q \\ r \end{bmatrix} \quad (11)$$

Roll damping moment:

$$\vec{M}_{rd} = \frac{1}{2} \rho S d V^2 C_{lp} \left(\frac{pd}{V} \right) \begin{bmatrix} 1 \\ 0 \\ 0 \end{bmatrix} \quad (12)$$

Incidence angle α and sideslip angle β are then defined by:

$$\tan \alpha = \frac{w}{u} \quad (13)$$

$$\tan \beta = \frac{v}{\sqrt{u^2 + w^2}} \quad (14)$$

Equations (1) to (4) apply for any kind of (rigid body) flying vehicle. Hence, the inertia matrix involved in equation (1) can be generally written as:

$$[I] = \begin{bmatrix} I_x & -I_{xy} & -I_{xz} \\ -I_{yx} & I_y & -I_{yz} \\ -I_{zx} & -I_{zy} & I_z \end{bmatrix} \quad (15)$$

Although the quaternion - form of these equations are used for 6DoF simulations, here we consider the Euler angles - form in order to introduce more easily the convenient non-rolling frames.

B. Non-rolling body frames BFP and BNS

By using the notations detailed in Fig. 1, the rotational velocity vector of a frame can very generally be written as (subscript F for Frame)⁸ :

$$\vec{\omega}_F = \dot{\phi}_F \vec{x}_3 + \dot{\theta} \vec{y}_2 + \dot{\psi} \vec{z}_1 \quad (16)$$

$$\vec{\omega}_F = p_F \vec{x}_{BR} + q_F \vec{y}_{BR} + r_F \vec{z}_{BR} \quad (17)$$

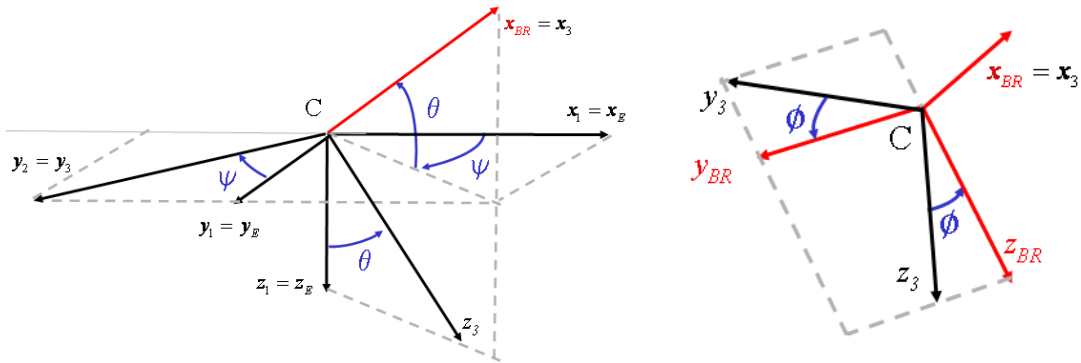


Figure 1: Euler angles ψ , θ and ϕ .

Hence, a frame experiencing the pitching and yawing rotational motions, but not the rolling motion can be characterized by:

$$\dot{\phi}_F = 0 \quad \text{or} \quad p_F = 0$$

This leads to two convenient non-rolling body frames :

- the *BFP* (Body Fixed Plane) frame defined by $\dot{\phi}_{F,BFP} = 0$
- the *BNS* (Body Non Spinning) frame defined by $p_{F,BNS} = 0$

C. Flight mechanics 6 DoF model in the non-rolling BFP frame

Assuming, with no loss of generality, that $\phi_{F,BFP}(0) = 0$, the condition $\dot{\phi}_{F,BFP} = 0$ obviously leads to $\phi_{F,BFP} = 0$. The consequence is that the \bar{y}_{BFP} axis of the BFP frame always remains in the Earth horizontal plane which is an interesting property, especially for guidance purposes. From equation (2) we have, for the BFP frame:

$$\dot{\phi}_{F,BFP} = p_{F,BFP} + q \sin \phi_{F,BFP} \tan \theta + r \cos \phi_{F,BFP} \tan \theta \quad (18)$$

Substituting $\dot{\phi}_{F,BFP} = \phi_{F,BFP} = 0$, we find^{8,9}:

$$p_{F,BFP} = -r \tan \theta \quad (19)$$

This is the spin rate of the BFP frame which ensures that the \bar{y}_{BFP} axis always remains in the Earth horizontal plane. As a consequence, the equations of motion are written, in the BFP frame, as^{8,9,10}:

$$\begin{bmatrix} \dot{p} \\ \dot{q} \\ \dot{r} \end{bmatrix} = [I]^{-1} \left(\begin{bmatrix} L \\ M \\ N \end{bmatrix} - \begin{bmatrix} 0 & -r & q \\ r & 0 & r \tan \theta \\ -q & -r \tan \theta & 0 \end{bmatrix} [I] \begin{bmatrix} p \\ q \\ r \end{bmatrix} \right) \quad (20)$$

$$\begin{bmatrix} \dot{\theta} \\ \dot{\psi} \end{bmatrix} = \begin{bmatrix} 0 & 1 & 0 \\ 0 & 0 & \frac{1}{\cos \theta} \end{bmatrix} \begin{bmatrix} p \\ q \\ r \end{bmatrix} \quad (21)$$

$$\begin{bmatrix} \dot{u} \\ \dot{v} \\ \dot{w} \end{bmatrix} = \begin{bmatrix} X/m \\ Y/m \\ Z/m \end{bmatrix} + g \begin{bmatrix} -\sin \theta \\ 0 \\ \cos \theta \end{bmatrix} - \begin{bmatrix} 0 & -r & q \\ r & 0 & r \tan \theta \\ -q & -r \tan \theta & 0 \end{bmatrix} \begin{bmatrix} u \\ v \\ w \end{bmatrix} \quad (22)$$

$$\begin{bmatrix} \dot{x}_E \\ \dot{y}_E \\ \dot{z}_E \end{bmatrix} = \begin{bmatrix} \cos \theta \cos \psi & -\sin \psi & \sin \theta \cos \psi \\ \cos \theta \sin \psi & \cos \psi & \sin \theta \sin \psi \\ -\sin \theta & 0 & \cos \theta \end{bmatrix} \begin{bmatrix} u \\ v \\ w \end{bmatrix} \quad (23)$$

The set of aerodynamic forces and moments equations is identical to the relations used for the body rolling frame (equations (6) to (14)) but the variables (incidence and sideslip angles, angular rates, ...) involved in these relations are now calculated in the BFP frame.

D. Flight mechanics 6 DoF model in the non-rolling BNS frame

The *BNS* frame is characterized by $p_{F,BNS} = 0$. As a consequence, the \bar{y}_{BNS} axis of the BNS frame is not located inside the Earth horizontal plane. The equations of motion are written, in the non-spinning body frame BNS, as⁸:

$$\begin{bmatrix} \dot{p} \\ \dot{q} \\ \dot{r} \end{bmatrix} = [I]^{-1} \left(\begin{bmatrix} L \\ M \\ N \end{bmatrix} - \begin{bmatrix} 0 & -r & q \\ r & 0 & 0 \\ -q & 0 & 0 \end{bmatrix} [I] \begin{bmatrix} p \\ q \\ r \end{bmatrix} \right) \quad (24)$$

$$\begin{bmatrix} \dot{\phi}_{F,BNS} \\ \dot{\theta} \\ \dot{\psi} \end{bmatrix} = \begin{bmatrix} 1 & \sin \phi_{F,BNS} \tan \theta & \cos \phi_{F,BNS} \tan \theta \\ 0 & \cos \phi_{F,BNS} & -\sin \phi_{F,BNS} \\ 0 & \frac{\sin \phi_{F,BNS}}{\cos \theta} & \frac{\cos \phi_{F,BNS}}{\cos \theta} \end{bmatrix} \begin{bmatrix} 0 \\ q \\ r \end{bmatrix} \quad (25)$$

$$\begin{bmatrix} \dot{u} \\ \dot{v} \\ \dot{w} \end{bmatrix} = \begin{bmatrix} X/m \\ Y/m \\ Z/m \end{bmatrix} + g \begin{bmatrix} -\sin \theta \\ \cos \theta \sin \phi_{F,BNS} \\ \cos \theta \cos \phi_{F,BNS} \end{bmatrix} - \begin{bmatrix} 0 & -r & q \\ r & 0 & 0 \\ -q & 0 & 0 \end{bmatrix} \begin{bmatrix} u \\ v \\ w \end{bmatrix} \quad (26)$$

$$\begin{bmatrix} \dot{x}_E \\ \dot{y}_E \\ \dot{z}_E \end{bmatrix} = \begin{bmatrix} \cos \theta \cos \psi & \sin \phi_{F,BNS} \sin \theta \cos \psi - \cos \phi_{F,BNS} \sin \psi & \cos \phi_{F,BNS} \sin \theta \cos \psi + \sin \phi_{F,BNS} \sin \psi \\ \cos \theta \sin \psi & \sin \phi_{F,BNS} \sin \theta \sin \psi + \cos \phi_{F,BNS} \cos \psi & \cos \phi_{F,BNS} \sin \theta \sin \psi - \sin \phi_{F,BNS} \cos \psi \\ -\sin \theta & \sin \phi_{F,BNS} \cos \theta & \cos \phi_{F,BNS} \cos \theta \end{bmatrix} \begin{bmatrix} u \\ v \\ w \end{bmatrix} \quad (27)$$

The set of aerodynamic forces and moments equations is identical to the relations used for the body rolling frame (equations (6) to (14)) but the variables (incidence and sideslip angles, angular rates, ...) involved in these relations are now calculated in the BNS frame.

E. Remarks concerning the BFP and BNS non-rolling frames

In assessing the relative merits of the different frames, one should consider the following points:

- The simulation time (CPU) is known to be directly dependent on the highest natural frequency of the system, which is here given by the roll angle variations in the BR frame. As can be seen from relations (20) to (23) and (24) to (27), the 6DoF equations in the BFP and BNS frames no longer depend on the projectile roll angle ϕ . Hence, the simulation time step is now function of the dynamics of the lateral axes, whose angular rates are much lower than the spin rate. As a consequence, much larger time steps can be used leading to significant savings in simulation time (see section IV.G).
- Even if the projectile roll angle is no more directly computed, it can be evaluated *a posteriori* (at the end of the 6DoF simulation). By using the first line of the reverse form of equation (2), the projectile roll angle is estimated in the BFP and BNS frames by⁸:

$$\phi(t) = \int_0^t (p + \dot{\psi} \sin \theta) d\tau \quad (28)$$

The accuracy of this estimation is illustrated in section IV.D.

- In the BFP and BNS frames, the projectile roll angle can be estimated *a posteriori* (at the end of the 6DoF simulation) if the inertia matrix is independent of the projectile roll angle. Hence, a diagonal inertia matrix is required :

$$[I]_{BFP}, [I]_{BNS} = \begin{bmatrix} I_x & 0 & 0 \\ 0 & I & 0 \\ 0 & 0 & I \end{bmatrix} \quad (29)$$

III. Polar diagram

A. Aeroballistics incidence polar diagram

From an historical point of view, our knowledge concerning flight dynamics of gun-launched projectiles has been mainly developed by using aeroballistics 6DoF models^{11,12,13}. These aeroballistics 6DoF models differ somewhat from the standard flight mechanics 6DoF models.

A very useful tool for analysing flight dynamics aspects of spin-stabilized projectiles is the so-called (aeroballistics) incidence polar diagram. This diagram represents the trace of the projectile nose in a plane perpendicular to the projectile's velocity vector. This plane is defined by vectors (\vec{h}, \vec{s}) with \vec{h} in the horizontal Earth plane and \vec{s} in the vertical Earth plan (Fig. 2). It is seen on Fig. 2 that the polar diagram depends on two angles: the total incidence

angle δ_b and the precession angle ψ_b . The interesting point is that some of these aeroballistics 6DoF models^{11,12} are designed in such a way that these two angles are variables of the simulation and hence, are directly calculated.

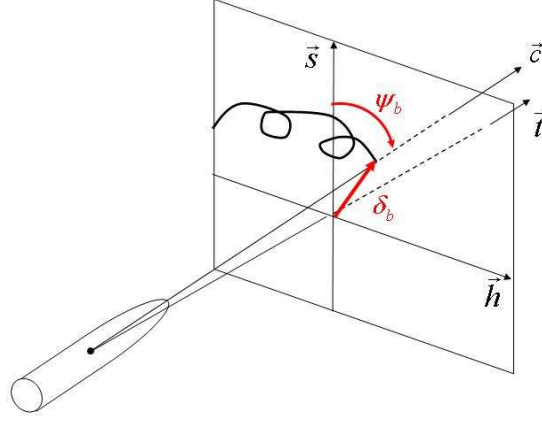


Figure 2: Aeroballistic incidence polar diagram
 \vec{h} is in the horizontal Earth plane, \vec{s} is in the vertical Earth plane
 \vec{t} is collinear to the velocity vector, \vec{c} is the projectile's longitudinal axis

B. Polar diagram in the rolling body frame BR

When using the rolling body frame BR, the incidence polar diagram can not be plotted immediately because the total incidence angle δ_b and the precession angle ψ_b are not directly calculated. Hence, it is necessary to derive relations between the (δ_b, ψ_b) angles and the flight mechanics angles⁸ :

Total incidence angle δ_b

The total incidence angle δ_b is simply calculated by:

$$\sin \delta_b = \sqrt{(\cos \beta \sin \alpha)^2 + (\sin \beta)^2} \quad (30)$$

Precession angle ψ_b

Two different methods can be used to derive expressions for the precession angle⁸. The resulting relations are the following:

Method 1:

$$\psi_b = \text{atan} \left(\frac{\sin \psi_b}{\cos \psi_b} \right) \quad (31)$$

with :

$$\sin \psi_b = \frac{\cos \theta \cos \psi \sin \eta_b + \cos \theta \sin \psi \cos \eta_b}{\sin \delta_b} \quad (32a)$$

$$\cos \psi_b = \frac{-\cos \theta \cos \psi \cos \eta_b \sin \theta_b + \sin \theta \cos \theta_b + \cos \theta \sin \psi \sin \eta_b \sin \theta_b}{\sin \delta_b} \quad (32b)$$

$$\eta_b = -\text{atan} \left(\frac{v_E}{u_E} \right) \quad (33)$$

$$\theta_b = \text{atan} \left(\frac{-w_E}{\sqrt{u_E^2 + v_E^2}} \right) \quad (34)$$

Method 2: in the approximation of small incidence angles, one can find the following relations:

$$\cos \psi_b = \frac{\sin \alpha \cdot \cos \phi + \sin \beta \cdot \cos \alpha \cdot \sin \phi}{\sqrt{(\cos \beta \sin \alpha)^2 + (\sin \beta)^2}} \quad (35)$$

$$\sin \psi_b = \frac{\sin \alpha \cdot \sin \phi - \sin \beta \cdot \cos \alpha \cdot \cos \phi}{\sqrt{(\cos \beta \sin \alpha)^2 + (\sin \beta)^2}} \quad (36)$$

C. Incidence polar diagram in the non-rolling BFP frame

When comparing the aeroballistics frames used in References 11, 12 and the BFP frame, we see that vectors \vec{h} and \vec{y}_{BFP} are equal. Hence, by comparing Fig. 2 and Fig 3, we conclude that, in the approximation of small incidence angles, the incidence polar diagram can be directly represented by the angles $-\beta_{M,BFP} \cong -\beta_{BFP}$ and $+\alpha_{BFP}$ (where $\tan \beta_M = \frac{\tan \beta}{\cos \alpha}$). This result also justifies the use of the BFP frame for the analysis of flight properties of spin-stabilized projectiles⁸.

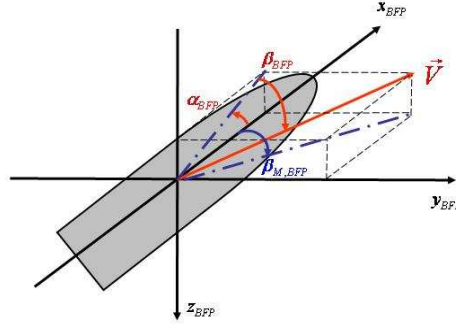


Figure 3 : Angles α_{BFP} , β_{BFP} and $\beta_{M,BFP}$

IV. Simulation results for a ballistic 155 mm projectile

A. Simulation conditions

We consider the case of a spin-stabilized 155 mm gun-launched projectile with a high initial elevation angle. The chosen initial conditions are (with respect to Earth frame):

- Initial body location: $(x_{E0}, y_{E0}, z_{E0}) = (0, 0, 0)$ in m
- Initial linear body velocity: $(u_{BR0}, v_{BR0}, w_{BR0}) = (800.0, 0, 0)$ in m/s
- Initial Euler angles: $(\psi_0, \theta_0, \phi_0) = (0, 63.0, 0)$ in degree
- Initial rotational body velocity: $(p_0, q_0, r_0) = (1600.0, 0, -3.5)$ in radian/s

B. Projectile flight kinematics and dynamics

In this section, we show different figures representing :

- the body locations (trajectory) in Earth frame: Fig. 4,
- the body linear velocities in Earth frame: Fig. 5,
- the body azimuth (yaw) and elevation (pitch) Euler angles in Earth frame: Fig. 6.
- the incidence and sideslip angles: Fig. 7,
- the body angular rates: Fig. 8.

For each figure, 6DoF simulations have been performed in different body frames (rolling BR, non-rolling BFP and BNS frames) and the results are compared with the results given by the reference code QFW (also developed at ISL). The following remarks can be made:

- Figure 4 shows an important lateral deviation of more than 1200 meters, a common feature for spin-stabilized projectiles. This deviation is discussed in section IV.E.
- Figures 4 to 6 show a perfect coherence for the simulations performed in the different body frames.
- Figures 7 and 8: High frequencies are visible on the figures concerning incidence and sideslip angles (Fig. 7) and body angular rates (Fig. 8) when the simulations are performed in the rolling frame BR. These high frequencies are of course related to the projectile roll motion and do not appear on the curves obtained in the non-rolling BFP and BNS frames. A slight difference between the BFP and BNS curves is observed which is due to the difference in the definitions of the two frames. In the rolling frame BR, the incidence and sideslip angles curves are seen to be 90° out-of-phase as expected.

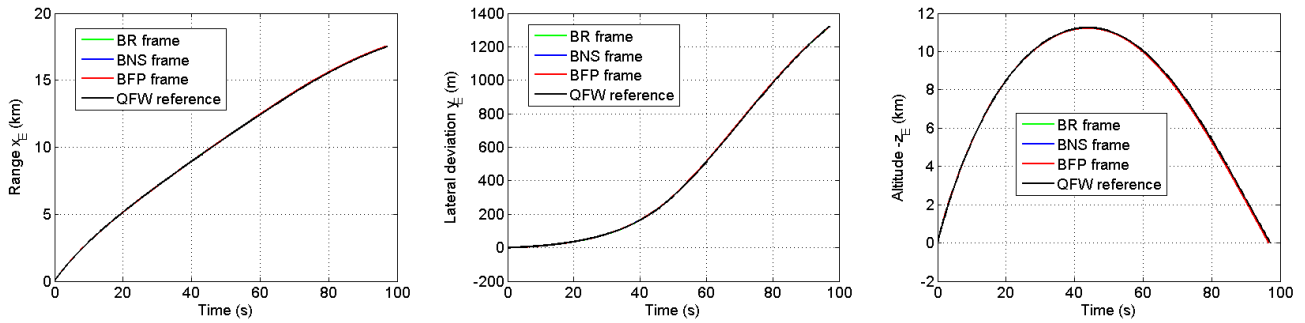


Figure 4: Body locations (trajectory)

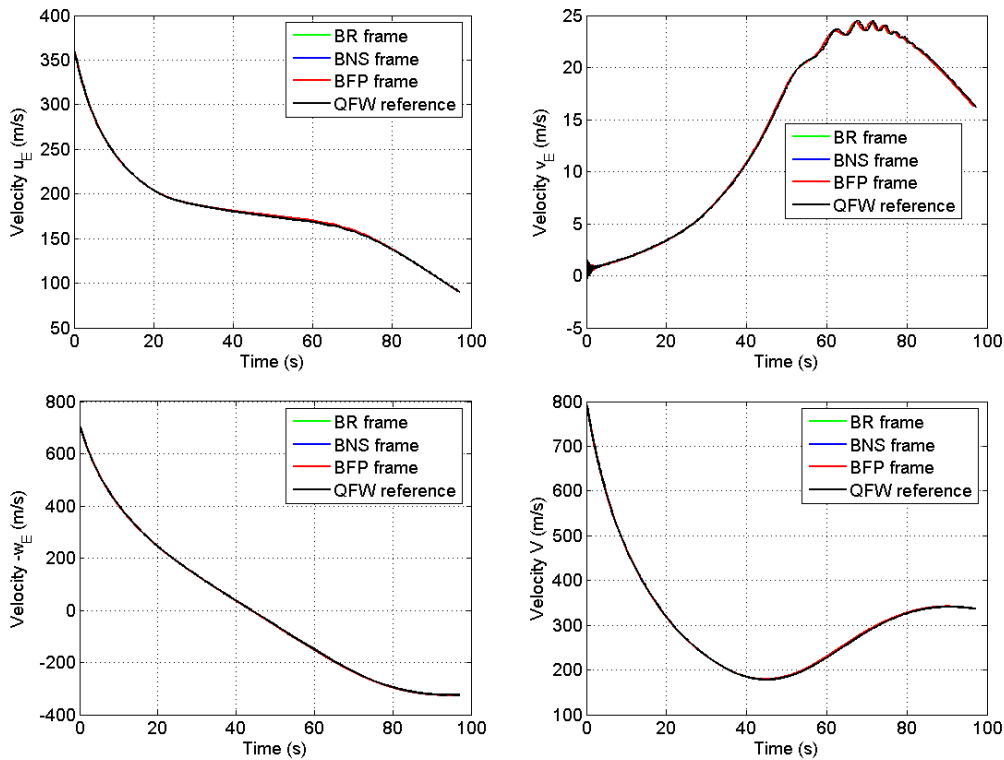


Figure 5: Body linear velocities

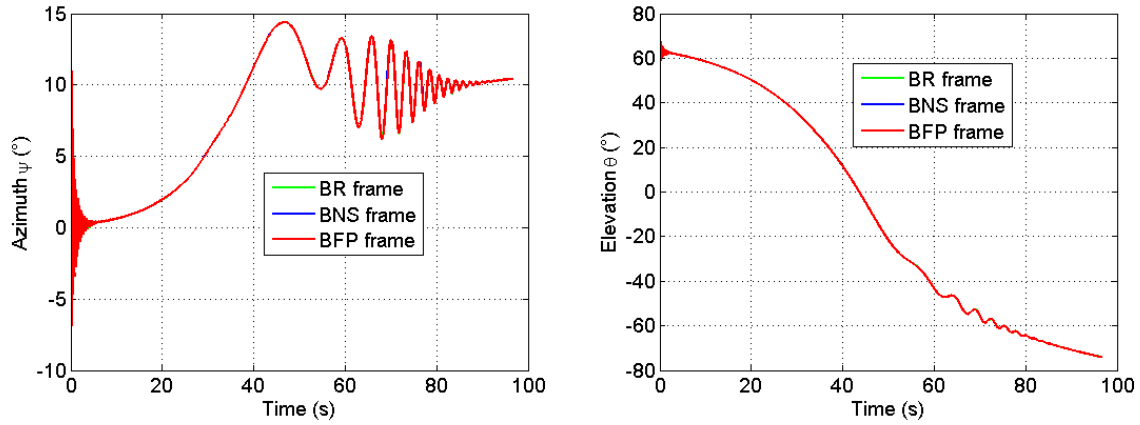


Figure 6: Azimuth (yaw) and elevation (pitch) Euler angles

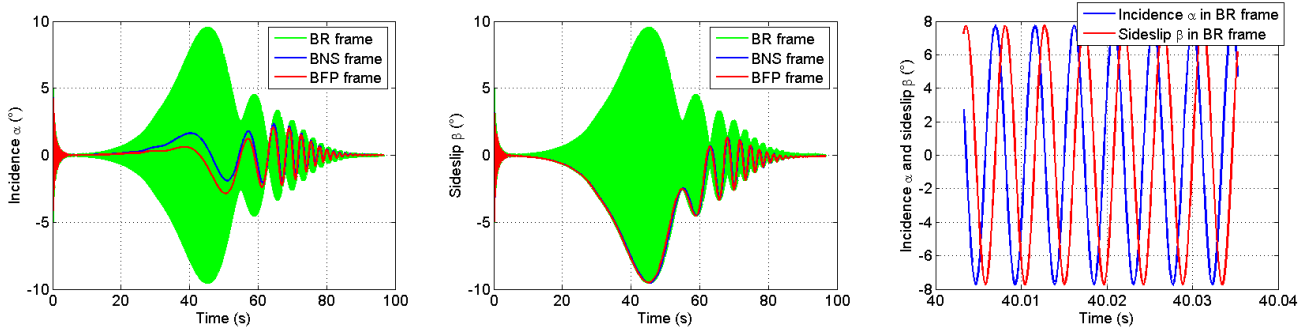


Figure 7: Incidence and sideslip angles

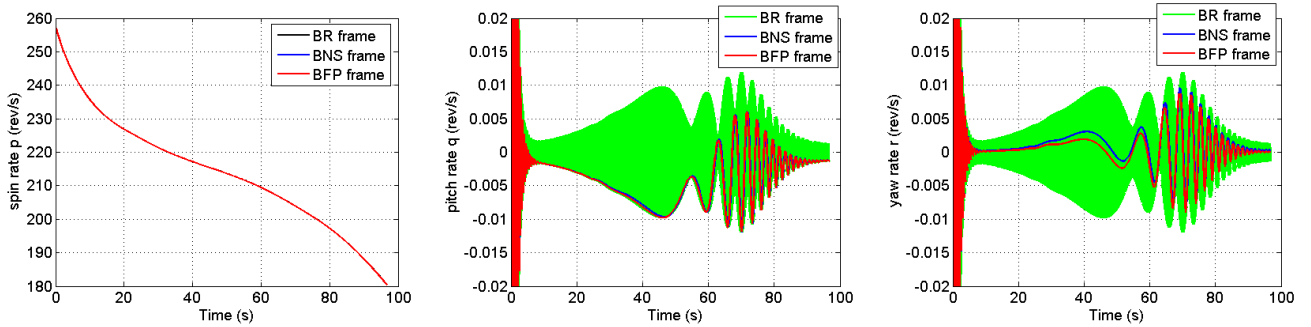


Figure 8: Body angular rates

C. Dynamics of THE non-rolling BFP and BNS frames

Figure 9 shows the time histories of the BFP and BNS frames roll angles. The relation $\phi_{F,BFP} = 0$ (resulting from condition $p_{F,BFP} = -r \tan \theta$, equation (19)) is obtained with a very good approximation, except two unexplained numerical artefacts and numerical transient effects whose magnitude depends on the numerical integration scheme. The BNS frame bank (roll) angle is seen to have non negligible variations (roll angles of more than 10°).

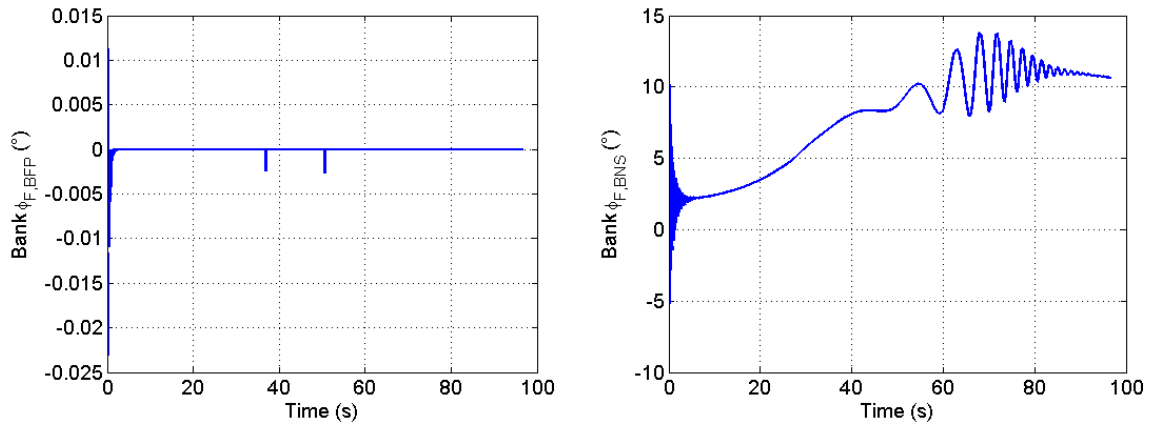


Figure 9 : BFP and BNS frames bank (roll) angles

Figure 10 shows the time histories of the BFP and BNS frames roll rates. The condition $p_{F,BNS} = 0$ is of course perfectly achieved (it is an input data).

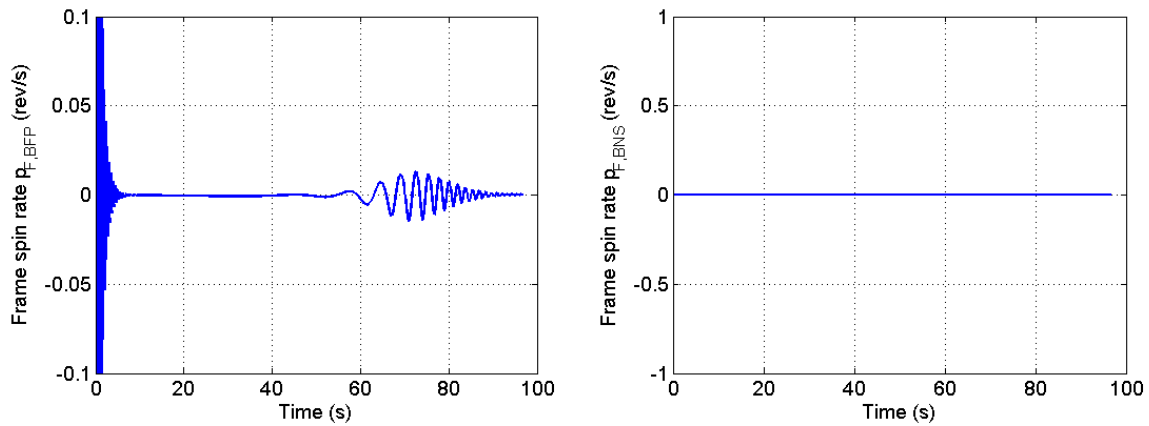


Figure 10: BFP and BNS frames roll rates

D. Reconstruction of projectile roll angle

As shown in section II.E, the projectile bank (roll) angle can be estimated *a posteriori* (at the end of the 6DoF simulation) in the BFP and BNS frames by using the following relation:

$$\phi(t) = \int_0^t (p + \dot{\psi} \sin \theta) d\tau \quad (28)$$

Figure 11 shows the time histories of the projectile roll angle in the rolling BR and fixed plane BFP frames. The aspect of the projectile roll angle curve estimated in the BFP frame is of course due to the time integration in the above mentioned relation (equation (28)). By projecting back into the $[-\pi, +\pi]$ interval, one obtains the results shown in Fig. 12. This figure shows that the reconstructed roll angle (calculated in the body fixed plane BFP frame) is in very good agreement with the roll angle directly calculated in the body rolling frame BR. However, discrepancies (due to numerical integration effects) can appear at the end of the simulation. Hence, an adapted numerical integration scheme must be used if reconstruction of roll angle is to be performed over a long time span.

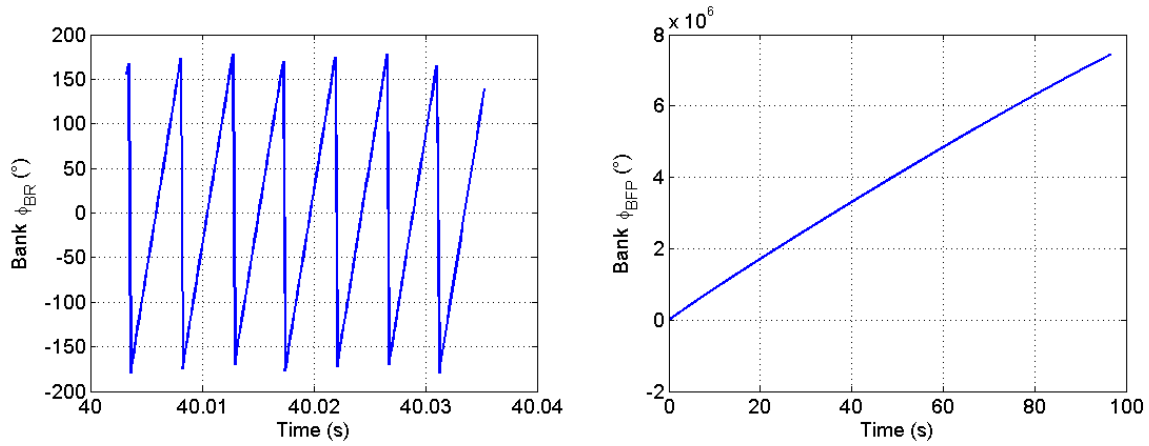


Figure 11 : Projectile roll angle in the rolling BR (left) and fixed plane BFP frames (right)

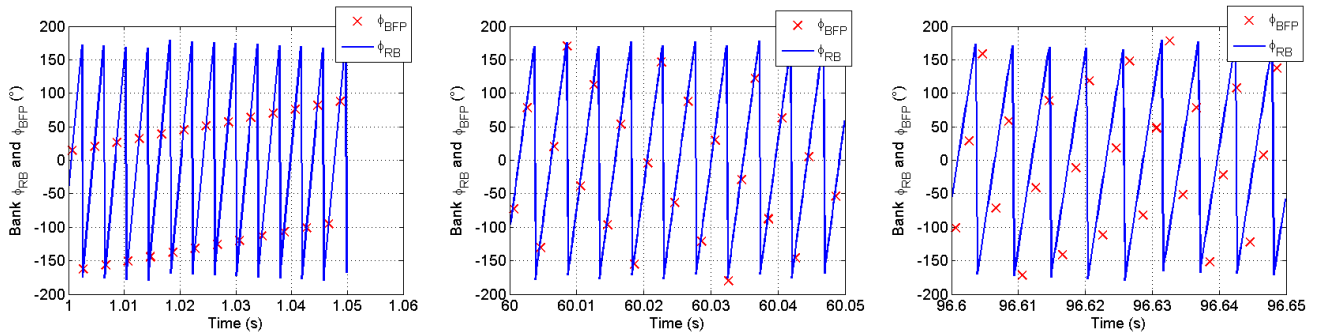


Figure 12 : True and reconstructed projectile bank (roll) angles at different flight instants.

E. Incidence polar diagrams

Figure 13 shows the time dependence of the total incidence angle δ_b and the precession angle ψ_b by using equations (30) to (34) for the body rolling BR frame and the calculated incidence and sideslip angles in the body fixed plane BFP frame (see section III.B and III.C).

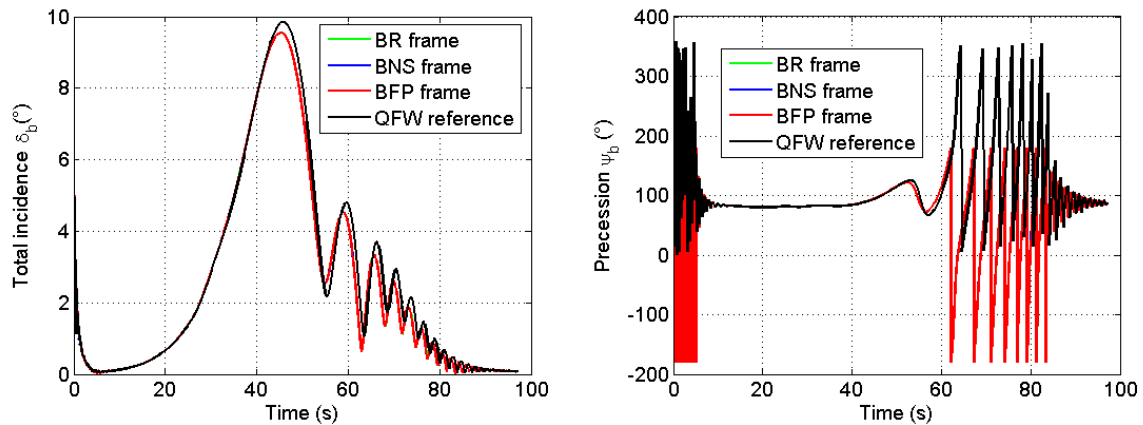


Figure 13 : Total incidence angle δ_b and precession angle ψ_b .

The following remarks can be made concerning Fig. 13:

- The precession angle ψ_b has been defined, in the different frames, with different intervals ($[0, 2\pi]$ or $[-\pi, +\pi]$).
- The precession angle ψ_b is seen to have an approximate constant value of about 80° for $10 < t < 40$ (s). Hence, by recalling Fig. 3, it can be concluded that the projectile exhibits a sideslip angle during about one third of the flight duration. Combined with the normal force on the projectile, this sideslip angle is responsible for the observed lateral deviation (see Fig. 4).

Figure 14 shows the incidence polar diagram resulting from Fig. 13. Again, a quasi perfect agreement between the two curves is observed.

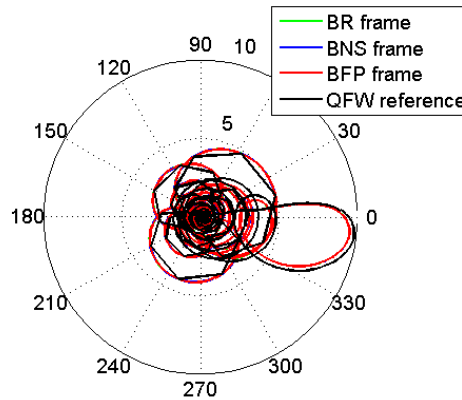


Figure 14 : Incidence polar diagram resulting from Fig. 13.

As Fig. 14 is difficult to analyze, the incidence polar diagram is split into four different flight phases as shown in Fig. 15. The explanations for these different flight stages are the following:

- For $0 \leq t \leq 0.4$ (s), typical precession/nutation pattern due to initial perturbations induced by gun launch.
- For $0.4 \leq t \leq 17$ (s), damping of initial perturbations (stabilization).
- For $17 \leq t \leq 75$ (s), dynamically unstable flight stage resulting in increasing total incidence. As noted on Fig. 13, Fig. 15c clearly shows that we mainly observe a sideslip angle (up to nearly 10°) rather than an incidence angle. This sideslip angle induces an important normal force (directed in the horizontal Earth plane) which results in the observed lateral deviation (Fig. 4).
- For $75 \leq t \leq 95$ (s), restabilization. In some cases, depending on flight conditions (wind) and modeling (damping and Magnus aerodynamics coefficients), this restabilization phase can be followed, during the very last few seconds, by a new dynamically unstable flight stage (not visible on Fig. 14d).

It must be noted that these observed stable and unstable flight stages are perfectly explained by using standard aeroballistics stability theories^{2,11,12,13}.

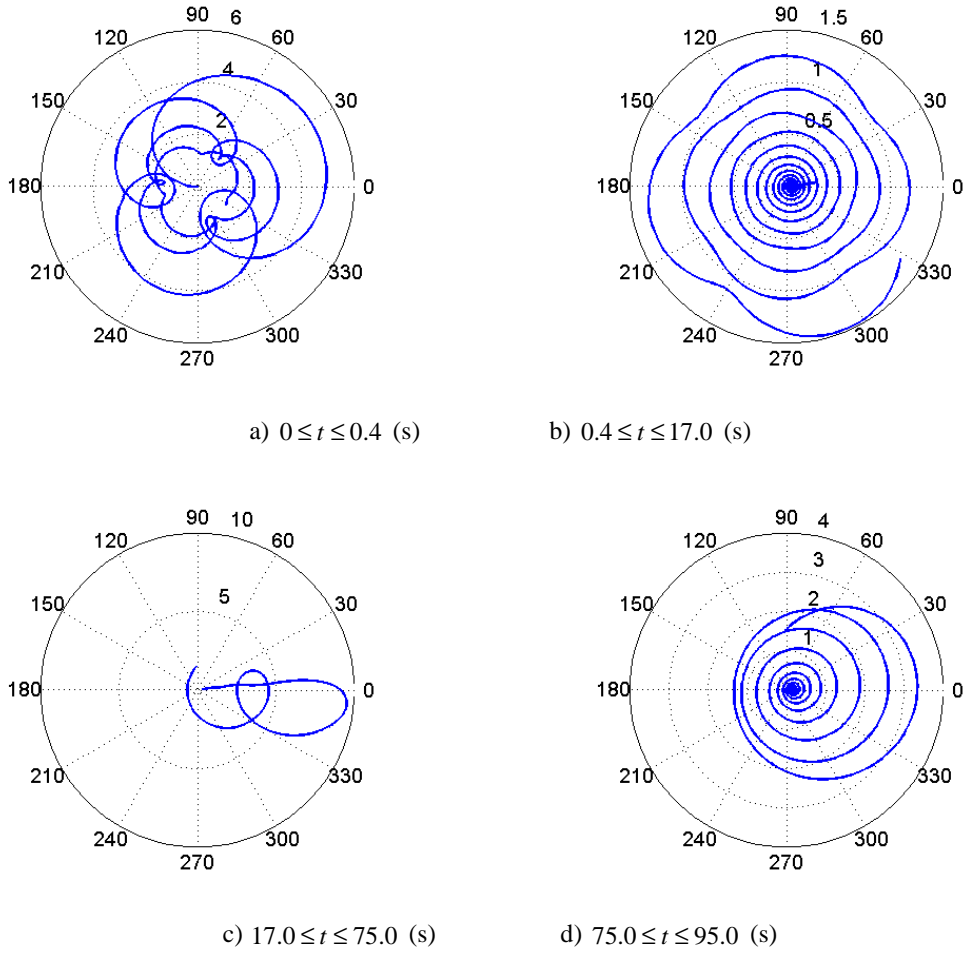


Figure 15 : Incidence polar diagram of Fig. 14 (results from the BFP frame) split into four different flight phases.

F. Forces and Moments

Figures 16 to 19 show time histories for individual and total forces and moments in the BR and BFP frames. The total forces and moments on the projectile will be written as:

- Total force : $\vec{F} = \vec{G} + \vec{L} + \vec{D} + \vec{K}$
- Total moment : $\vec{M} = \vec{M}_{py} + \vec{M}_m + \vec{M}_{pyd} + \vec{M}_{rd}$

Forces and moments in the body rolling frame BR

Figure 16 shows the evolution of the forces in the body rolling frame BR.

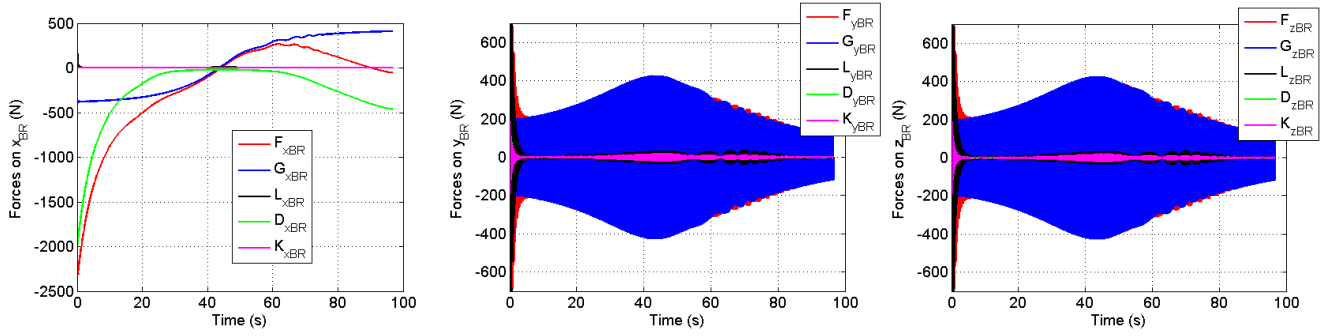


Figure 16 : Forces in the body rolling frame BR

In a similar fashion, figure 17 shows the evolution of the moments in the body rolling frame BR.

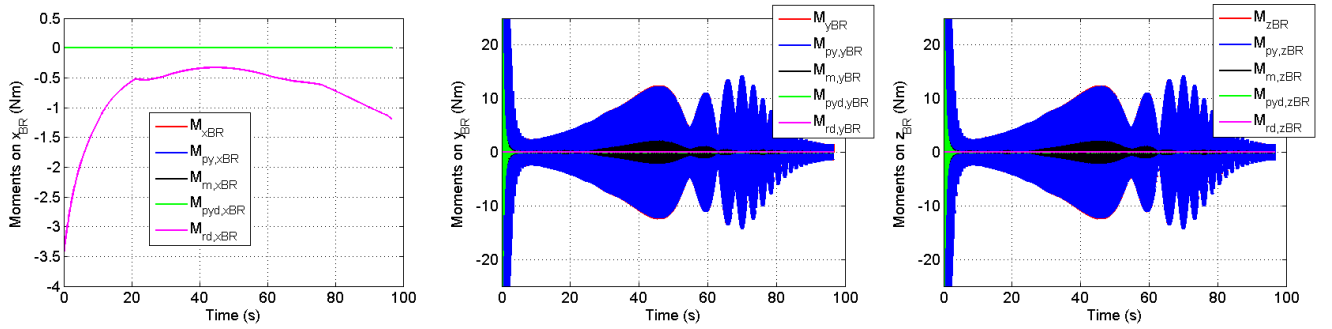


Figure 17 : Moments in the body rolling frame BR

On both figures 16 and 17, the evident non-oscillatory shape of the forces and moments on the x_B axis and the evident oscillatory shape of the forces and moments on the y_B et z_B axes are clearly visible.

Forces and moments in the body fixed plane frame BFP

Figure 18 shows the evolution of the forces in the body fixed plane frame BFP.

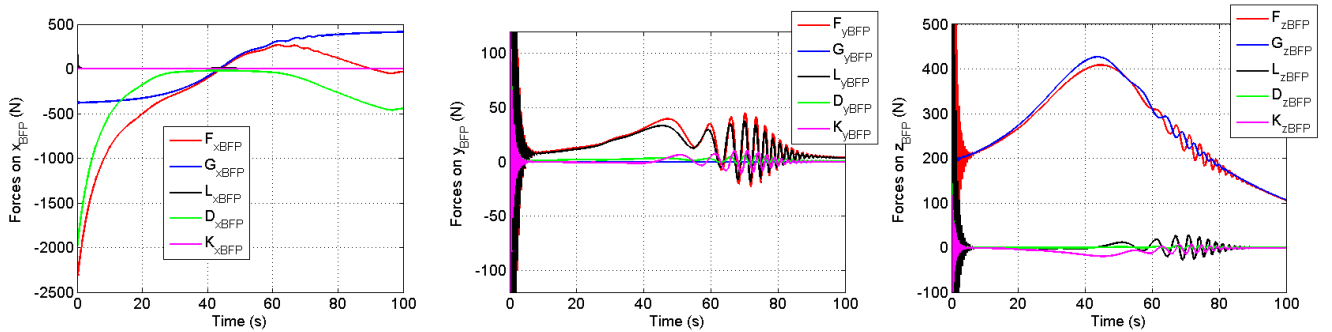


Figure 18: Forces in the body fixed plane frame BFP

Following remarks can be made concerning Figure 18:

- On the x_{BFP} axis: the drag D_{xBFP} and gravity G_{xBFP} forces are the most important forces,
- On the y_{BFP} axis: the total force F_{yBFP} is almost completely due to the lift component L_{yBFP} . Hence, the lateral deviation of the projectile (on the y_{BFP} axis) is mainly due to the lift force (and the sideslip angle, cf Fig. 15c) but the Magnus force K_{yBFP} can not be neglected,
- On the z_{BFP} axis: the total force F_{zBFP} is almost completely due to the gravity force G_{zBFP} .

Figure 19 shows the evolution of the moments in the body fixed plane frame BFP.

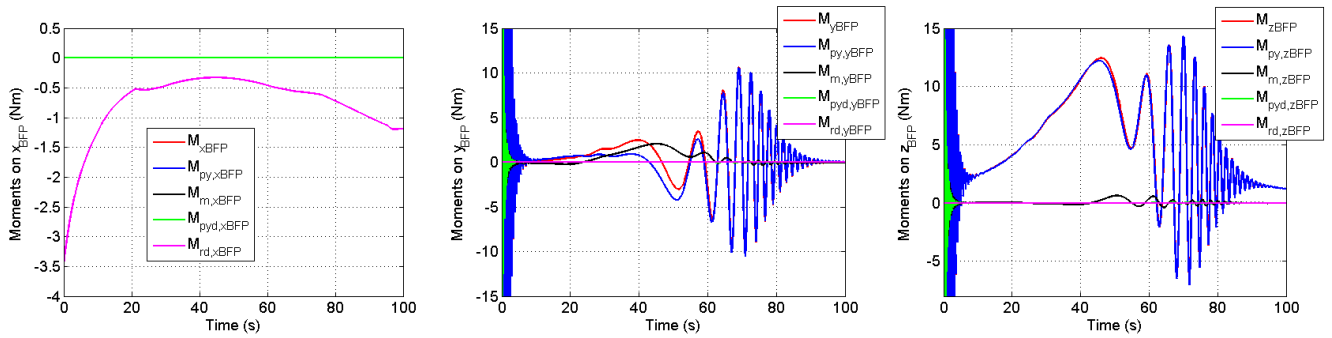


Figure 19: Moments in the body fixed plane frame BFP

Following remarks can be made concerning Figure 19:

- On the x_{BFP} axis: the only non-zero moment is the roll damping moment,
- On the y_{BFP} axis: after the first flight seconds, the main moments are the pitch-yaw moment $M_{py,yBFP}$ and the Magnus moment $M_{m,yBFP}$. Near the apogee (flight time between 30s and 50s), the Magnus moment is seen to be of same order of magnitude as the pitch-yaw moment.
- On the z_{BFP} axis: the total force M_{zBFP} is almost completely due to the pitch-yaw moment $M_{py,zBFP}$.

G. Step size and CPU time

When performing multiple simulations (Monte-Carlo simulations with hundreds or thousands of runs), CPU time is a problem of concern. As an illustration, the following results concern one single run for a complete trajectory and have been obtained with average personal computers and a Matlab-Simulink program using the ODE113 solver.

Body Spinning Frame BR

- Steps : about 500 000
- Mean step size : about 2.10^{-4} s
- CPU time : 30 s - 2 minutes

Body Fixed Plane Frame BFP

- Steps : about 10 000
- Mean step size : about 10^{-2} s
- CPU time : 1-3 secondes

However, in the BFP frame, with a mean step size of about 10^{-2} s, some too large numerical errors can appear. A good trade-off between accuracy and CPU time is obtained with:

- Steps : about 50 000
- Mean step size : about 2.10^{-3} s
- CPU time : 3-10 secondes

Hence, it can be seen that the use of a non-rolling frame (here the BFP frame) drastically reduces the time span needed to perform Monte-Carlo simulations. As an illustration, Fig. 20 shows the typical evolution of time step sizes for the rolling BR and the non-rolling BFP frames.

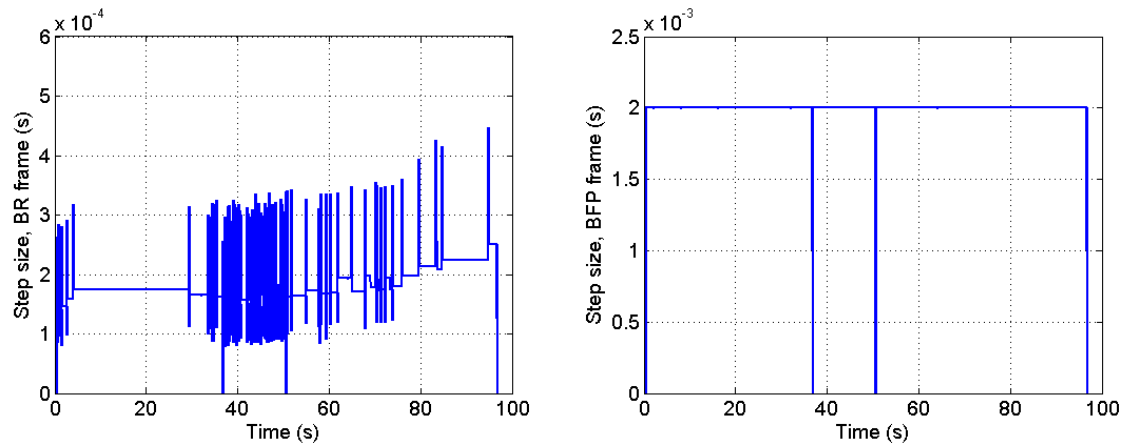


Figure 20 : Step sizes

Conclusions

The most significant points in this paper are the following:

- The sets of equations needed to perform trajectory simulations for gun launched, spin-stabilized 155 mm projectiles have been detailed in different body frames (rolling BR and non-rolling BFP and BNS frames).
- The simulation results (in the different body frames) concerning kinematics and dynamics data are in very close agreement.
- The incidence polar diagram, an essential figure to understand the projectile's flight behaviour, can be obtained from simulations performed in the different body frames. When using the BFP frame, the incidence polar diagram is directly obtained (in the approximation of small incidence angles).
- The use of a non-rolling frame (here the BFP frame) drastically reduces the time span needed to perform Monte-Carlo simulations, in general without loss of accuracy. This is due to the fact that the projectile roll angle no more needs to be directly calculated. Hence, it can be evaluated *a posteriori* (at the end of the 6DoF simulation). However, some discrepancies (due to numerical integration effects) can appear at the end of the simulation.

Finally, it can be noted that, as the \vec{y}_{BFP} axis of the BFP frame always remains in the Earth horizontal plane, the body fixed plane BFP frame a very convenient frame for the study of concepts of guided ammunitions or missiles^{4,5,9,10}.

References

- ¹Wernert P., Leopold F., Bidino D., Juncker J., Lehmann L. Bär K. and Reindler A., Wind tunnel tests and open-loop trajectory simulations for a 155 mm canards guided spin stabilized projectile, *AIAA Atmospheric Flight Mechanics Conference and Exhibit*, 18-21 August 2008, Honolulu, Hawaii, AIAA Paper 2008-6881.
- ²Wernert P., Stability analysis for canard guided dual-spin stabilized projectiles, *AIAA Atmospheric Flight Mechanics Conference and Exhibit*, 10-13 August 2009, Chicago, Illinois, AIAA Paper 2009-5843.
- ³Theodoulis S., Morel Y., Wernert P., Trajectory based accurate linearization of the 155mm spin-stabilized projectile dynamics, *AIAA Atmospheric Flight Mechanics Conference and Exhibit*, 10-13 August 2009, Chicago, Illinois, AIAA Paper 2009-6236.
- ⁴Theodoulis S., Morel Y., Wernert P., Modelling and stability analysis of the 155mm spin-stabilized projectile equipped with steering fins, *International Journal of Modelling, Identification and Control*, under review.
- ⁵Theodoulis S., Morel Y., Wernert P., LPV modelling of guided projectiles for terminal guidance, *18th Mediterranean Conference on Control and Automation*, June 23-25, 2010, Marrakech (Marocco).
- ⁶Wernert P., "Simulations de trajectoires de projectiles à six degrés de liberté dans le cadre de la mécanique du vol avion. Partie 1: Mise en équation et résolution par la méthode des quaternions", ISL Report R 123/2004, 2004.
- ⁷Wernert P., "Simulations de trajectoires de projectiles à six degrés de liberté dans le cadre de la mécanique du vol avion. Partie 2: Validation dans le cas d'un projectile empenné de calibre 38 mm et d'un projectile gyroscopé de calibre 155 mm", ISL Report R 131/2005, 2005.
- ⁸Wernert P., "Simulations de trajectoires de projectiles à six degrés de liberté dans le cadre de la mécanique du vol avion. Partie 3: Utilisation de repères non liés au projectile", ISL Report R 124/2007, 2007.
- ⁹Lloyd K.H. and Brown D.P., "Instability of Spinning Projectiles During Terminal Guidance", *Journal of Guidance and Control*, Vol. 2, N° 1, 1979, pp. 65-70.
- ¹⁰Costello M. and Peterson A., Linear theory of a dual-spin projectile in atmospheric flight, *Journal of Guidance and Control*, Vol. 23, N° 5, 2000, pp. 789-797.
- ¹¹Molitz H. and Strobel R., *Äussere Ballistik*, Springer Verlag, Berlin, 1963.
- ¹²Fleck V., *Cours de ballistique extérieure*, ENSIETA, Brest, 1997.
- ¹³McCoy R.L., *Modern Exterior Ballistics*, Schiffer Ed., Atglen, PA, 1999.